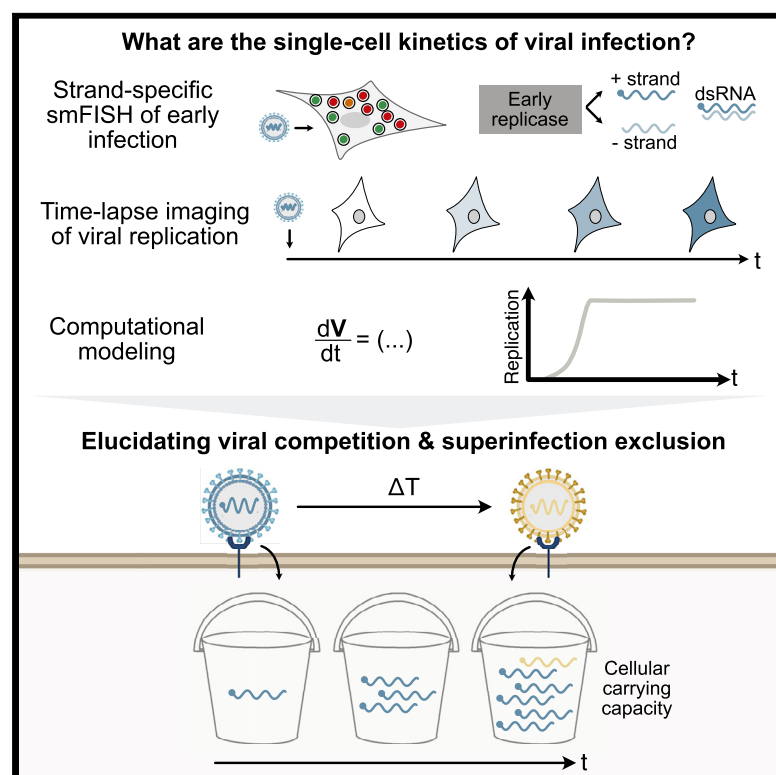# Quantitative measurements of early alphaviral replication dynamics in single cells reveals the basis for superinfection exclusion

Graphical Abstract

What are the single-cell kinetics of viral infection?

Strand-specific smFISH of early infection

Early replicase

+ strand
dsRNA
- strand

Time-lapse imaging of viral replication

t

Computational modeling

$$\frac{d\mathbf{V}}{dt} = (...)$$

Replication

t

Elucidating viral competition & superinfection exclusion

ΔT

Cellular carrying capacity

t

Authors

Zakary S. Singer, Pradeep M. Ambrose, Tal Danino, Charles M. Rice

Correspondence

td2506@columbia.edu (T.D.), ricec@rockefeller.edu (C.M.R.)

In Brief

Singer et al. utilize quantitative single-cell and single-molecule methods to investigate the earliest events of alphaviral replication biology. Through measurements of viral kinetics at the RNA and protein levels, they reveal the trajectory of viral replication. Applying this approach in the context of viral competition reveals that the rapid kinetics of viral replication with a limited cellular carrying capacity are able to explain the long-observed phenomenon of alphaviral superinfection exclusion.

Highlights

- Single-molecule FISH and time-lapse imaging of alphavirus infection kinetics

- Early replicase synthesizes plus- and minus-strand viral RNAs at an equal rate

- Infection kinetics of single cells over time reveal stereotyped logistic growth

- Superinfection exclusion is a bidirectional competition under limited resources

Cell Systems

CellPress

Article

Quantitative measurements of early alphaviral replication dynamics in single cells reveals the basis for superinfection exclusion

Zakary S. Singer,[1,2] Pradeep M. Ambrose,[2,3] Tal Danino,[1,4,5,*] and Charles M. Rice[2,6,*]
[1]Department of Biomedical Engineering, Columbia University, New York, NY 10027, USA
[2]Laboratory of Virology and Infectious Disease, The Rockefeller University, New York, NY 10065, USA
[3]Department of Physiology, Biophysics, and Systems Biology, Weill Cornell Medicine, New York, NY 10065, USA
[4]Herbert Irving Comprehensive Cancer Center, Columbia University, New York, NY 10027, USA
[5]Data Science Institute, Columbia University, New York, NY 10027, USA
[6]Lead contact
*Correspondence: td2506@columbia.edu (T.D.), ricec@rockefeller.edu (C.M.R.)
https://doi.org/10.1016/j.cels.2020.12.005

SUMMARY

While decades of research have elucidated many steps of the alphavirus lifecycle, the earliest replication dynamics have remained unclear. This missing time window has obscured early replicase strand-synthesis behavior and prevented elucidation of how the first events of infection might influence subsequent viral competition. Using quantitative live-cell and single-molecule imaging, we observed the initial replicase activity and its strand preferences in situ and measured the trajectory of replication over time. Under this quantitative framework, we investigated viral competition, where one alphavirus is able to exclude superinfection by a second homologous virus. We show that this appears as an indirect phenotypic consequence of a bidirectional competition between the two species, coupled with the rapid onset of viral replication and a limited total cellular carrying capacity. Together, these results emphasize the utility of analyzing viral kinetics within single cells.

INTRODUCTION

Sindbis virus is a plus-strand RNA virus with a broad host range that cycles between vertebrate and mosquito hosts (Strauss and Strauss, 1994). As the type virus of the alphavirus genus, its replication has been studied in detail since its discovery in 1953 (Taylor and Hurlbut, 1953; Taylor et al., 1955). Upon release into a cell, the infecting plus strand is translated as a large polyprotein that contains the replication machinery (Figure 1). Polyprotein processing through cleavage is tightly regulated, where differential cleavage between early and late infection are thought to alter the template preferences of the replicase. This progression has been suggested to cause a transition from minus-strand production to plus-strand replication and finally to subgenomic transcription, with the latter encoding the viral structural proteins (de Groot et al., 1990; Sawicki et al., 1990; Lemm and Rice, 1993a, 1993b; Sawicki and Sawicki, 1993; Lemm et al., 1994; Shirako and Strauss, 1994).

Across both prokaryotes and eukaryotes, a phenomenon know as superinfection exclusion (SE) has been observed, where infection by one virus can block replication of a subsequent homologous virus (Dulbecco, 1952a; Steck and Rubin, 1966; Bratt and Rubin, 1968; Whitaker-Dowling et al., 1983; Johnson and Spear, 1989; Lee et al., 2005; Zou et al., 2009; Biryukov and

Meyers, 2018). In principle, such a behavior could serve to improve dissemination by preventing reinfection of already infected cells and protect a virus from competing with its progeny or a similar superinfecting virus. One potential mechanism of action is limiting a second virus's entry through down-regulation or depletion of receptors or even repulsion of virions away from the surface of infected cells (Garcia and Miller, 1991; Huang et al., 2008; Stiles et al., 2008; Doceul et al., 2010). The changes required in cellular state to achieve this are generally thought to occur over the course of several hours following infection. However, for alphaviruses like Sindbis virus, such a phenomenon can be seen within just 15 minutes of the first infection, leading to a reduction in the titer of the second alphavirus by an order of magnitude (Johnston et al., 1974; Adams and Brown, 1985; Karpf et al., 1997; Singh et al., 1997).

Even though this rapid competitive behavior was observed for Sindbis over 40 years ago, its origins have remained elusive. Moreover, despite elegant studies revealing the lifecycle of alphaviruses, our understanding of the earliest stages of replication and the specific events establishing such a rapid exclusionary environment are unclear. For example, population-level measurements have revealed the accumulation of plus- and minus-strand RNA and concomitant processing of viral polyprotein over the first ~3–6 hours post infection (hpi) and the first
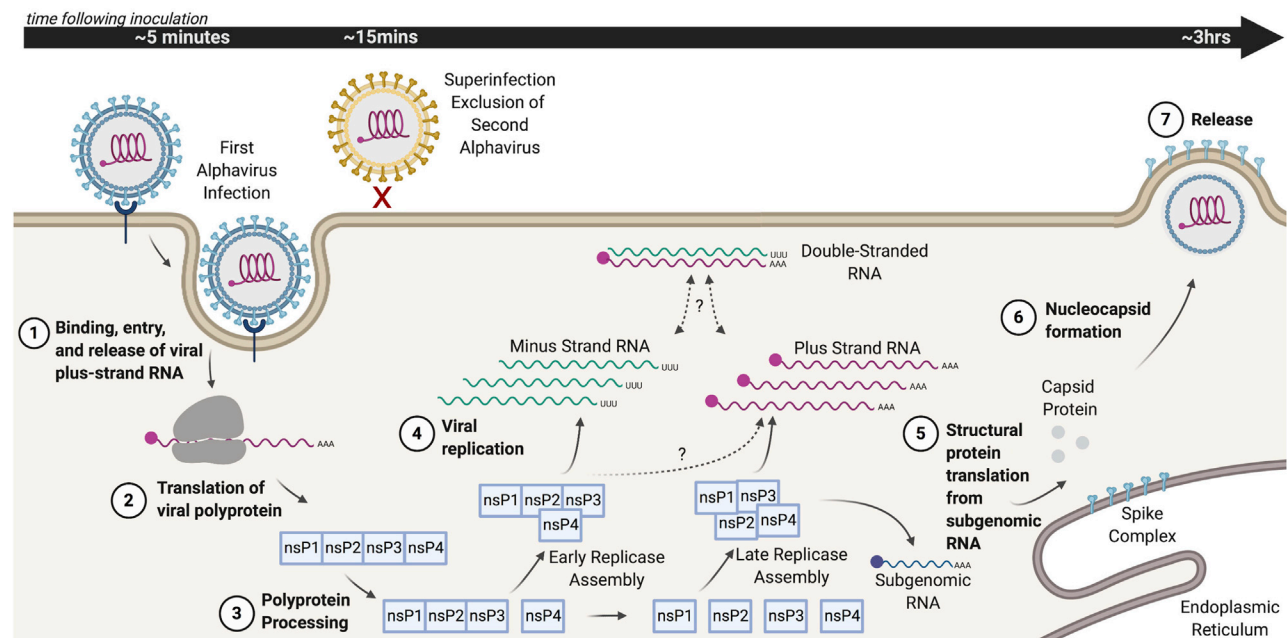
Figure 1. Overview of the alphavirus lifecycle

Alphaviruses enter via receptor-mediated endocytosis, after which the viral plus-strand genome is released into the host cytoplasm. This genome also serves as an mRNA, enabling translation of the viral polyproteins P123 and P1234, which include the non-structural proteins, nsP1, nsP2, nsP3, and nsP4. Polyprotein P1234 is first cleaved in *cis* to liberate nsP4, the RNA-dependent RNA polymerase. Early forms of the replicase are thought to contain P123 and nsP4, while the late replicase is composed of fully cleaved nsP1-4. This continued cleavage over time has been shown to influence transitions in production between the full-length minus-strand intermediate, the genomic plus strand, and the subgenomic RNA. The subgenomic RNA encodes the structural proteins, Capsid, PE2, and E1 that are required for subsequent nucleocapsid assembly and release. The replication kinetics of these different vRNAs at the single-cell level, the early replicase polarity, and how these contribute to the rapid exclusion of a superinfecting alphavirus have all remained unclear.

release of progeny virions as early as ~3–4 hpi(Sawicki and Sawicki, 1980; Sawicki et al., 1981; Strauss and Strauss, 1994). However, it is unknown when the very first minus strand is produced, whether the early replicase prefers to synthesize plus- or minus-strand RNA within the first few hours of replication, and how such early replicase behaviors might contribute to SE.

A major challenge in the study of early replication dynamics and how these behaviors might influence competitive interactions has been the use of population-based measurements, which lack the sensitivity to investigate low-abundance targets during early infection. While classic studies have shown the average growth of the virus over time across millions of cells, the underlying growth kinetics that contribute to this mean, and how the inherent cell-to-cell variability and unsynchronized nature of a spreading infection might obscure these measurements are still unknown. For example, does the virus grow constantly and linearly in a subpopulation or grow exponentially and then plateau in some cells and decay over time in others? A quantitative analysis of early replicase activity and the ability to follow the time course in single cells could elucidate the underlying nature of viral replication and reveal events on the timescale during which SE behaviors emerge.

The use of single-cell analyses in biology have enabled an unprecedented look into the behavior of natural genetic circuits, in part, by revealing how the variability of individual cells can be masked by the overall population's behavior (Fraser and Kaern, 2009; Locke and Elowitz, 2009; Raj and van Oudenaarden, 2009; Chalancon et al., 2012). The use of single-cell approaches in

virology has only recently begun to show how variability between individual cells contribute to viral growth and spreading kinetics, how stochasticity can influence fate selection in both phages and animal viruses, and how quantitative models might lead to improved antivirals (Snijder et al., 2009; Doceul et al., 2010; Jones et al., 2010; Zeng et al., 2010; Chou et al., 2012; Schulte and Andino, 2014; Heldt et al., 2015; Razooky et al., 2015; Akpinar et al., 2016; Ramanan et al., 2016; Guo et al., 2017; Hansen et al., 2018; Drayman et al., 2019; Shnayder et al., 2020). In this study, by directly exploring the progression of viral replicase activity *in situ* and the resulting single-cell replication kinetics, we shed light on classic questions remaining in alphavirology and provide a new framework for understanding early replication and the resulting exclusionary phenomenon.

RESULTS

Strand-specific single-molecule measurements during early viral RNA synthesis

In order to capture the dynamics of the earliest stages of replication, it is necessary to utilize an approach with high enough sensitivity to simultaneously measure individual molecules of multiple viral RNA (vRNA) species at low abundance. Furthermore, the methods must permit investigation at the single-cell level, in order for the resulting measurements to reveal potential heterogeneity among the population, such as a refractory subset of cells or an unsynchronized infection from spatial and temporal waves of spreading. Single-molecule RNA fluorescence *in situ*
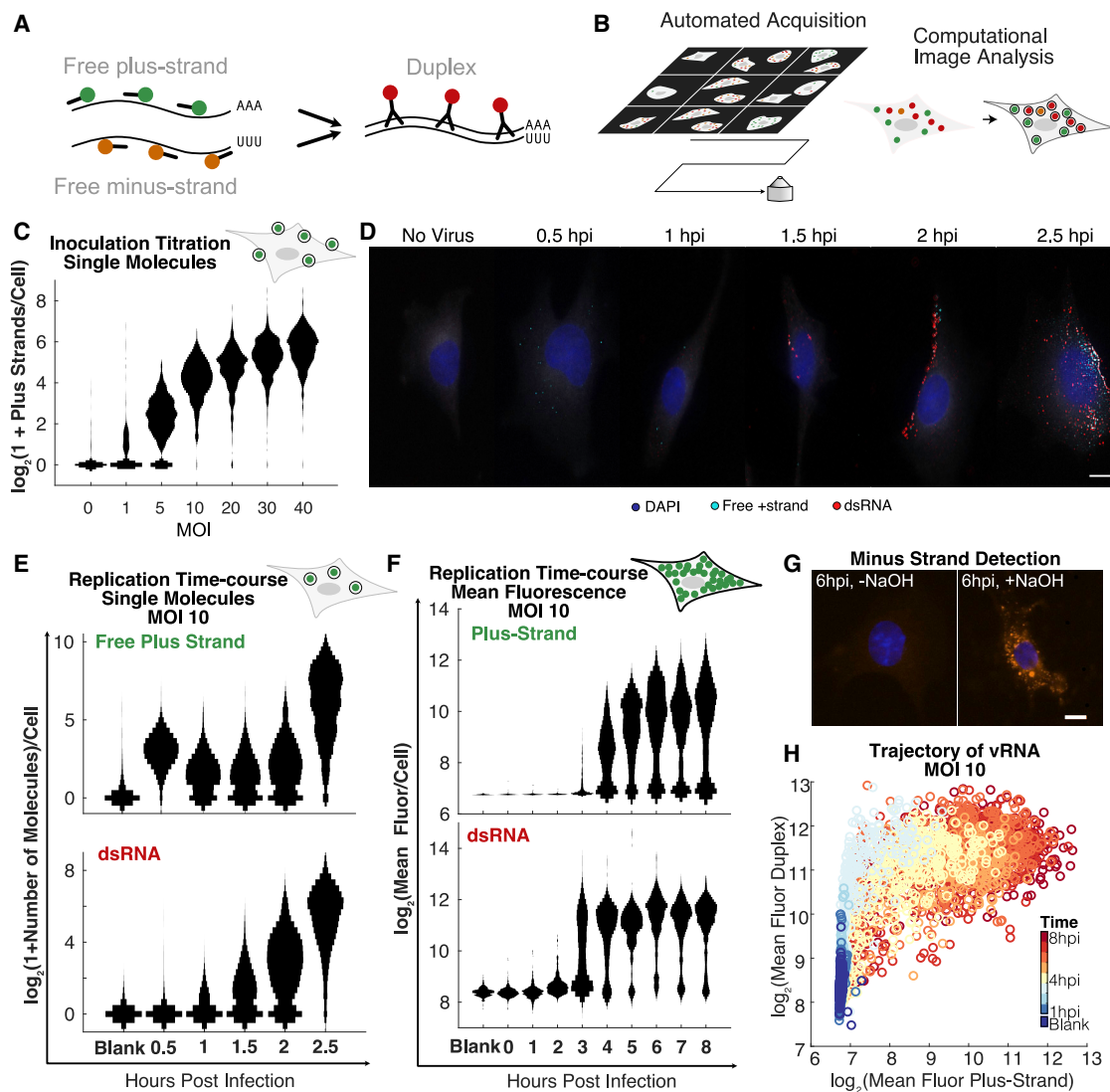
Cell Systems
Article

CellPress

Figure 2. Trajectories of Sindbis vRNA by strand-specific immunoFISH

(A) Schematic showing the immunoFISH strand-specific probes against free plus and minus strands, as well as immunostaining of dsRNA by J2 antibodies, each chromatically distinct from one another.

(B) Grid-based acquisition is performed automatically on the microscope (left), followed by automated cell segmentation and dot detection analysis (right).

(C) Counts of single spots of virions per cell immediately following inoculation, over a range of MOIs, displayed as smoothened vertical histograms.

(D) Representative images of infected cells, co-stained for dsRNA and free plus-strand RNA through 2.5 hpi. Blue, DAPI; white, cytoplasm; cyan, free plus strand; red, dsRNA. Scale bar is 10 μm.

(E) Counts of spots in individual cells of free plus strand (top) and dsRNA (bottom) over a time course through 2.5 hpi, displayed as smoothened vertical histograms.

(F) Distributions of total fluorescence per cell from free plus strand (top) and dsRNA (bottom) over an 8-h time course.

(G) Minus-strand RNA only appears after treatment with NaOH (right) and not without (left), shown at 6 hpi. Scale bar is 10 μm.

(H) Single-cell scatter plot of total fluorescence per cell for dsRNA versus free plus-strand RNA, where the color represents the sample's time point.

hybridization (smFISH) can yield an assay in which the binding of multiple fluorescent probes to their target RNA creates discrete and countable diffraction-limited spots (Figure 2A). Furthermore, multiple chromatically distinct probe sets can be used in parallel to measure, with strand specificity, the abundance of the full-length genomic plus strand and its template, the minus strand. Based on the targeting of these probe sets to the sequence of the non-structural proteins, levels of subgenomic transcripts will not contribute to their signal. However, viral plus and minus

strands are entirely complementary to each other and potentially form a duplex that cannot be bound by small 20mer smFISH probes under standard hybridization conditions. Therefore, we additionally perform immunostaining in the same sample using an antibody that recognizes stretches of duplex or double-stranded RNA (dsRNA) longer than 40 base pairs (Schönborn et al., 1991). Together, with this immunoFISH approach, we are able to distinguish free plus and minus strands from the fraction of vRNA in duplex form, using automated image analysis to

detect and quantify these individual puncta within segmented cells (Figure 2B).

To establish the sensitivity of the method for detecting viral plus strands, we exposed BHK-21 cells to virus across a gradient of multiplicity of infections (MOIs) and fixed the cells immediately following a 30 minute inoculation (Figures 2C and S1A). At MOI 1, about half of all cells had detectable puncta of viral genomic RNA, with an average of 3.0 ± 3.7 per cell, while at MOI 10, nearly all cells had puncta, with an average of 19.9 ± 12.6 (mean $\pm$ SD). These measurements also revealed a surprising amount of variability between cells. Measures of dispersion such as the Fano factor (variance/mean) provide a way to compare variability between distributions. For a Poisson distribution, the Fano factor is 1. At MOI 10, the observed Fano factor is $7.9 = 1 \pm 0.8$ (mean $\pm$ SEM), suggesting a dispersion greater than what would be expected from a Poisson distribution (Ellis and Delbrück, 1939; Dulbecco, 1952b). Together, these results confirm the sensitivity of the approach and the ability to detect individual molecules of viral plus-strand RNA.

Next, we asked how the distributions of free plus and minus strands and duplex RNA evolved across the first 2.5 hpi, sampling cells at 30-min intervals (N = 3,553). Representative images are shown in Figure 2D. Intriguingly, the distribution of plus strands detectable immediately following the inoculation (0.5 hpi) was significantly reduced at 1 hpi (two-sample Kolmogorov-Smirnov [KS] test, $p = 1.49 \times 10^{-67}$), in conjunction with an increase in the first measurable duplex RNA (two-sample KS test, $p = 3.8 \times 10^{-16}$, Figure 2E). The emergence of duplex necessarily implies a corresponding production of minus-strand RNA from plus strand, detectable as dsRNA. Furthermore, while dsRNA continued to increase steadily over this interval, free plus strands did not. Between 2 and 2.5 hpi, however, there was a sudden and significant increase in both dsRNA and free plus strands and the abundance of plus strands thereafter exceeded the limit of individually quantifiable puncta.

Broadening the window of investigation, we measured hourly time points between 1 hpi and 8 hpi and quantified the resulting total fluorescence from plus-strand FISH and duplex-RNA immunostaining in a total of 4,555 cells (Figure 2F). Inspecting the temporal evolution of these distributions, a subpopulation of cells appeared to reach plateau levels of dsRNA as early as 3 hpi, while the signal from free plus-strand production appeared to continue in most cells for about two additional hours. This upper-bound in dsRNA abundance is likely a result of a so called "minus-strand shutoff," where the accumulated production of nsP2-protease leads to the cleavage of viral polyprotein into its constituent non-structural proteins, which form a replicase that is unable to produce additional minus strands (Sawicki and Sawicki, 1980; Lemm et al., 1994). Looking subcellularly, sites of dsRNA were concentrated most strongly along the boundary of the cell (Figure 2D), consistent with a model in which replication occurs within spherules along the plasma membrane throughout the full time course of infection (Froshauer et al., 1988; Frolova et al., 2010; Spuul et al., 2010). Notably, no free minus-strand RNA was ever observed (Figure S1B). To rule out the possibility that the lack of detectable free minus strand was caused by poor sensitivity of minus-strand probes, disruption of duplexes by sodium hydroxide was able to reveal minus-strand RNA (Figure 2G).

As these dsRNA and plus-strand measurements were performed simultaneously within the same cells, we could additionally explore the evolution of the "polarity" of the replicase activity for either making plus strand or minus strand (contained in duplex) over time. Plotting the single-cell measurements of total fluorescence of both vRNA species, color-coded by time, a trajectory of viral replication emerges in which plus and minus strands are first produced in nearly equal amounts, yielding duplex RNA. Only after significant levels of duplex RNA are established in a given cell does free plus strand emerge (Figures 2H and S1C).

Together, these single-molecule and total fluorescence measurements provide one of the earliest detections of alphaviral replication, revealing the initiation of replication within the first hour of infection. Furthermore, these results suggest a revised model of early replication wherein both plus- and minus strands are made at a similar rate during early infection—as opposed to a window that is biased toward minus-strand synthesis—where both full-length vRNAs can be utilized as templates during the first 2 h of infection.

Single-cell dynamics of viral replication

While smFISH provides a strand-specific view of replication at the level of the viral genome, the resulting kinetics are necessarily estimated from changes in distributions of cells taken at fixed time points and do not consider the proteins responsible for the observed dynamics. Thus, the ability to follow replication in single cells over time and at the protein level would serve to complement these static RNA snapshots.

In order to evaluate the early replication dynamics of Sindbis virus in live cells, we inserted the fluorescent protein mTurquoise2 gene into the hyper variable region of the non-structural protein, nsP3 (Figures 3A and 3B; Video S1), which we designate as SINV/nsP3-mTurquoise2. The fluorescence from this fusion reporter provides a direct readout of non-structural protein levels, while having minimal effect on viral replication (Jose et al., 2017). In order to first establish the relationship between the fluorescent reporter and vRNA, we simultaneously quantified nsP3-mTurquoise2 levels with vRNA by immunoFISH. Reporter fluorescent kinetics were similar to vRNA kinetics, plateauing at about 4 hpi at MOI 10, with individual puncta observable robustly at 1.5 hpi (Figures 3C and S2A). Comparing protein levels to vRNA, nsP3-mTurquoise2 appeared well correlated with dsRNA (Pearson correlation coefficient r = 0.92, Figure 3D) and just slightly less well correlated with free plus-strand RNA (Pearson correlation coefficient r = 0.90, Figure 3E). Together, this data suggest that vRNA and polyprotein levels increase with similar dynamics and that following nsP3-mTurquoise2 over time can serve as a proxy for the underlying RNA levels as well.

To analyze replication within single cells in real time, we adapted segmentation and tracking software based on nuclear fluorescence (Hormoz et al., 2016) to additionally follow cytoplasmic signals, where alphaviral replication occurs exclusively. This method yields a fluorescent "trace" for each cell that describes the temporal history of its nsP3-fused fluorescent reporter over the course of the experiment. We performed infections over a range of MOIs and asked whether and how replication dynamics differed between them. Traces of infected cells revealed
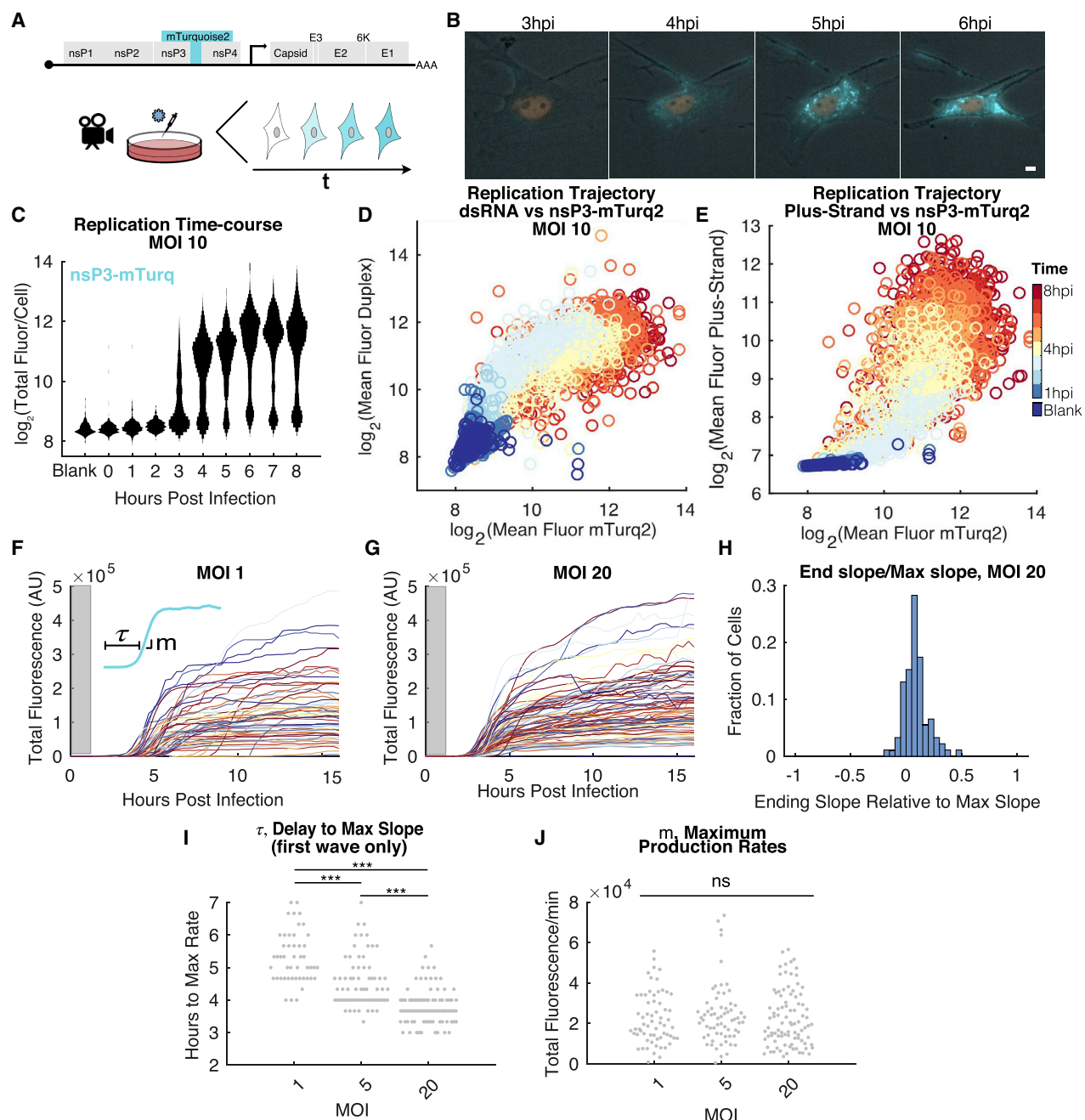
Cell Systems
Article

CellPress

Figure 3. Time-lapse microscopy reveals logistic growth of viral replication

(A) Schematic of viral reporter and experimental approach.

(B) Example multicolor images of the same cell over time with a nuclear stain (orange) and increasing levels of nsP3-mTurquoise2 (cyan). Scale bar is 10 μm.

(C) Single-cell distributions of total nsP3-mTurquoise2 normalized by area, plotted over time as vertical smoothened histograms.

(D) Scatter plot of total levels, normalized by area, of dsRNA versus nsP3-mTurquoise2, where each point is a single cell. Pearson correlation r=0.92. The color represents the sample's time point.

(E) Scatter plot of total levels, normalized by area, of plus-strand RNA versus nsP3-mTurquoise2, where each point is a single cell. Pearson correlation r=0.90. The color represents the sample's time point.

(F) Single-cell traces of total reporter-virus fluorescence infected at MOI 1. Gray box indicates the first hour during the inoculation and movie-preparation window before measurements were taken. Inset indicates τ, the time delay until the trace's maximum slope, m, on an example trace.

(G) Single-cell traces of total reporter virus fluorescence infected at MOI 20. Gray box indicates the first hour during the inoculation and movie-preparation window before measurements were taken.

(H) The fold reduction in slopes computed as the slope over the last 3 h of the traces fit to a line, divided by the maximum rate of change of the trace, shown for MOI 20 infection.

stereotyped logistic growth kinetics over all MOIs, where a sharp exponential increase in fluorescence was followed by a significantly reduced slope or a complete plateauing in production, similar to what was observed by immunoFISH (Figures 3F, 3G, and S2B). On average, the slope of the fluorescence over the last 5 h of the movie was reduced by 93% ± 5% (mean ± SD) relative to the maximal slope during early replication (Figures 3H and S2C). Additionally, metrics quantifying trace parameters such as the delay to the onset of exponential growth designated as τ and the maximum slope, m, can also be quantified and compared between conditions. While logistic growth appeared consistent across these conditions, the onset delays, τ, appeared to decrease with increasing MOIs (Figure 3I) and the maximum slope distributions appeared independent of MOI (Figure 3J).

One potential explanation for these stereotyped kinetics is that a host-cell shutoff might lead to diminished rates of replication or non-structural protein translation. To test if the kinetics are dominated by host-cell transcription and translation shutoff, we utilized a double mutant shown to abrogate these functions through point mutations in the nsP2 protease domain and nsP3 macrodomain, respectively (Akhrymuk et al., 2018). In this mutant there were little to no change in the qualitative stereotyped kinetics, suggesting that the observed growth was not mediated by these two host effects (Figure S2D).

Superinfection exclusion arising from logistic growth

What are the implications of these apparent timescales and logistic growth and how might it relate to observations of alphaviral competition? Previous work has shown that alphaviruses rapidly inhibit the replication of subsequent alphaviral infections in both mosquito and vertebrate cells, where this SE is independent of interferon and defective interfering particles (Zebovitz and Brown, 1968; Stollar and Shenk, 1973; Johnston et al., 1974; Igarashi et al., 1977; Adams and Brown, 1985; Karpf et al., 1997). For example, Sindbis virus has been shown to block infection by chikungunya, Una, Ross River, and Semliki Forest viruses, reducing their titer by between 2 and 5 orders of magnitude (Eaton, 1979; Karpf et al., 1997). Such work, however, has necessarily relied on indirect measurements of replication provided by plaque assays, in which the progeny of the two competing viruses were distinguished by characteristic differences in temperature sensitivity or by plaque size or shape. Thus, the relative competition and replication between the two viruses within the same cell at early times of infection have remained unclear. Although it has been previously shown that the inhibition of superinfection replication occurs post-entry (Adams and Brown, 1985), there has only been speculation about the potential sources of the blockade.

To examine some of the earliest events in the competition between two viruses in the same cell, we constructed a second reporter strain, replacing mTurquoise2 with the structurally nearly identical but chromatically distinct mCitrine protein. Using these two reporters, we systematically varied the interval between inoculation of the two viruses, as well as the MOI of the second virus. Specifically, the first virus, SINV/nsP3-mTurquoise2 was inoculated at an MOI 10 and was introduced either 0, 20, 40, or 60 min before the second virus, SINV/nsP3-mCitrine. This second virus was added at a range of MOIs (1, 5, 10, or 30), after which we recorded the resulting fluorescence from both viruses using single-cell time-lapse imaging. An example multicolor montage of the resulting infection at 12 hpi is shown in Figure 4A.

Instead of displaying a complete resistance to superinfection, infection by the second virus occurred in a manner dependent on both the delay and relative MOI between the two viruses; as the delay between the two increased or the MOI of the second virus was reduced, the ability of the second virus to replicate became further inhibited. This was reflected in both the mean fluorescence of the second virus SINV/nsP3-mCitrine in doubly infected cells as well as the fraction of cells detectably superinfected as measured by reporter-protein translation (Figures 4B–4D, and S3A).

Inspection of the traces following single cells during superinfection revealed further quantitative characteristics of the exclusionary phenomenon (Figures 4E–4G). If infection by the founding virus progressively created a less favorable environment for the second virus, perhaps the single-cell traces would reveal an effect on dynamics later during infection, such as a sudden shut off of replication. Instead, superinfection replication was apparently inhibited at the earliest stages, as the max replication rate m of the second virus was reduced, as opposed to a late effect during replication (Figure S3B).

To determine whether there might also be a bidirectional inhibition between the two viruses, we plotted the final levels of mTurquoise2 and mCitrine at 12 hpi across all temporal delays and superinfecting MOIs. We observed a strong anticorrelation between their endpoint fluorescence levels (Figures 4H and S3C, Pearson correlation coefficient r = −0.99), which suggests that the superinfecting virus is equally able to reduce replication levels of the first virus and that cells appear to have a fixed carrying capacity that determines the combined replication level of the two viruses.

Based on the observations of stereotypical growth dynamics, an early reduction in maximum production rates of the second virus during superinfection, and bidirectional interference during viral competition, we constructed a mathematical model of competitive Lotka-Volterra logistic growth using parameters estimated from single-virus infection experiments (Figure S3D, STAR methods). This form predicts that, due to the speed of Sindbis replication, any temporal delay or decrease in the relative MOI would strongly disadvantage the second virus. The model recapitulates the empirical measurements, wherein we observed a graded response in superinfection replication levels with increased delays, decreased relative MOI, and combinations thereof leading to a corresponding reduction in the second virus's replication (Figure 4I). Together, these data emphasize

---

(I) Distributions of the time delay, τ, in hours, as a function of MOI, where each gray dot is a cell. Comparing MOI 1 to MOI 5 distributions, significance by the non-parametric two-sample KS test is p = 3.4×10^{-7}. Comparing MOI 5 to MOI 20, p = 5.5×10^{-7}. Comparing MOI 1 to MOI 20, p = 1.98×10^{-19}.

(J) Distributions of the maximum production rates, m, as a function of MOI, where each gray dot is a cell. No comparisons are statistically significant by KS test.
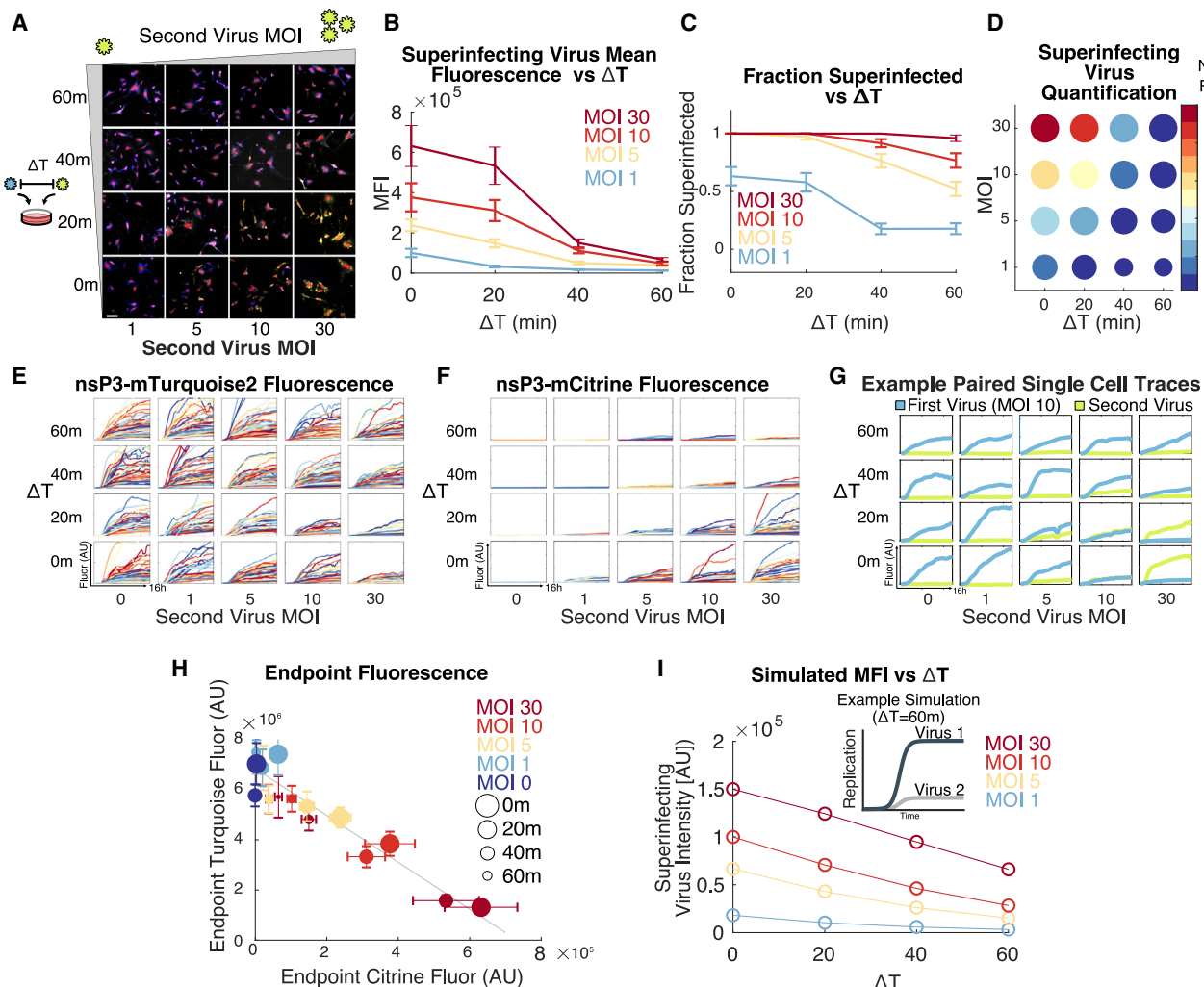
Figure 4. Single-cell measurements of SE reveal bidirectional viral competition

(A) Cells initially infected with MOI 10 of SINV/nsP3-mTurquoise2 were subsequently infected with SINV/nsP3-mCitrine at a range of MOIs (0, 5, 10, or 30) after different delays (either 0, 20, 40, or 60 m). Representative images show a nuclear stain (red), SINV/nsP3-mCitrine (yellow), and SINV/nsP3-mTurquoise2 (blue) under each described condition. Scale bar is 100 μm.

(B) Mean fluorescence per area (or MFI) averaged over all cells in the given condition as a function of delay (ΔT), shown as mean ± SEM. Color coding of each line represents a different superinfecting MOI.

(C) A plot of the fraction of cells infected by the second virus, SINV/nsP3-mCitrine as a function of delay (ΔT) and superinfecting MOI. Error bars are bootstrapped SEM.

(D) Information from (B) and (C) are combined to visually depict how temporal delays and relative MOIs together influence superinfection. Color represents the average fluorescence intensity normalized to the maximum across all conditions, while circle size represents the fraction of cells infected.

(E and F) Single-cell traces of replication kinetics from the first virus SINV/nsP3-mTurquoise2 (left), and the second virus SINV/nsP3-mCitrine (right) under the experimental conditions described in (A) through the 13-h time course. y axes of subplots in (E) are all equal, as are the y axes in (F). MOIs indicated are of the superinfecting SINV/nsP3-mCitrine. The first virus is always kept at MOI 10.

(G) Under superinfecting conditions, each panel shows an example pair of traces from both viral reporters in the same single cell, over time. To show both reporters on the same plot, y axes for mCitrine and mTurquoise2 are distinct in a given plot, but the ranges are constant across all panels. MOIs indicated along the bottom are of the superinfecting SINV/nsP3-mCitrine, while the first virus, SINV/nsP3-mTurquoise2, is kept at MOI 10. Each row is a fixed delay (ΔT) between the first and second virus. Analogous to Figures 4E and 4F.

(H) Total fluorescence averaged over single cells of nsP3-mTurquoise2 versus nsP3-mCitrine at the end of the superinfection movie (13 hpi) shown in (E) and (F). Circle size represents delay between the first and second viruses (ΔT) and color represents the MOI of the second virus, each shown as mean ± SEM. Gray line is a linear least squares fit, with a Pearson correlation coefficient r = −0.99.

(I) Lotka-Volterra simulations of the superinfection experiment where both the first and second viruses were modeled identically (r = 0.03/min and K = 200,000, see STAR methods) over a range of delays and superinfecting MOIs. Inset shows a model of viral replication kinetics, where both begin at MOI 10 but with ΔT = 20 min.

the importance of intrinsic growth kinetics in alphaviral superinfection exclusion.

DISCUSSION

While the complex choreography of polyprotein processing that controls the alphaviral lifecycle has been studied in detail, the early replicase activity and overall trajectory of vRNA synthesis *in situ* has remained unclear. In this study, we have sought to utilize single-cell imaging approaches in order to elucidate these phenomena and to determine how these give rise to SE.

Current models of replication for alphaviruses have suggested that immediately following release of the polymerase nsP4 from the polyprotein P1234 by *cis*-cleavage, P123+nsP4 preferentially acts as a minus-strand replicase. Reports are, however, conflicted regarding the activity of P123+nsP4 as a plus-strand replicase (Lemm et al., 1994; Shirako and Strauss, 1994). The results shown here appear to rule out a scenario where the production of minus strands is first heavily favored during early infection and instead suggests that polyprotein P123+nsP4 may additionally act as a plus-strand replicase early during infection, yielding a replicase with a "balanced polarity." This would be advantageous for the virus, as the early production of additional plus strands would accelerate the onset of the exponential phase of replication, especially when such kinetics appear closely related to SE. Live-cell microscopy further confirmed that the speed of this onset was dependent on the MOI, while the maximum slope was not, as a model of logistic growth would suggest. These single-cell traces uncovered the sharpness of exponential growth and subsequent plateau, which would have appeared shallower and delayed when averaging over such an unsynchronized population.

A mechanism that provides a competitive advantage over a similar secondary infection within a fraction of an hour could be broadly beneficial across a wide host range, especially considering the virus's ability to enter a cell within mere minutes (Helenius et al., 1980; Singh and Helenius, 1992). Using single-cell methods, we observed that the rapid onset of vRNA synthesis with balanced polarity could confer such an advantage. Such a passive SE mechanism may also shield the infecting virus from any of its mutated progeny that arise during naturally error-prone replication by the RNA-dependent RNA polymerase. Furthermore, a Lotka-Volterra model of exponential growth in a resource-limited environment appears consistent with empirical measurements of single and competitive viral replication and independent of mutations ablating host shutoff of transcription and translation (Akhrymuk et al., 2018). However, while these experiments suggest that a cell's carrying capacity may be responsible for the observed kinetics, the potential role of a "virus-intrinsic" program governing replication could also contribute to the logistic growth (Zeng et al., 2010; Razooky et al., 2015). Additionally, the apparent distribution in plateau levels of viral reporter fluorescence also highlights cell-to-cell differences and stochasticity in replication. The phenotypic state of cells and their spatial positions in culture have previously been shown to contribute to infection outcome (Snijder et al., 2009; Cohen and Kobiler, 2016). Such factors, potentially including a range of characteristics such as cell size, expression levels of key host factors, innate immune response, or transcriptional and translational capacity, can be considered together as an overall cellular state. Thus, the apparent "carrying capacity" of each cell is therefore likely an amalgamation of some or all of these effects. The results described here, following previous studies of SE in alphaviruses, have been performed in BHK cells, arguing against a role for innate immunity in this phenomenon. Indeed, should a host resource be the dominant component in limiting cellular capacity for alphaviral replication, its identification could potentially lead to a novel drug target against alphaviral replication.

A comparative and integrative view of cell state and innate immune activity in the context of viral replication *in situ* could reveal whether and how the observed dynamics may be further shaped by distinct immune responses between Sindbis virus's mosquito and vertebrate hosts and may also reveal differences in strategies used by the virus across these different organisms. As demonstrated here, single-cell imaging modalities can offer unique insight into classic questions of virology. As these methods are non-destructive, they are also suited to studying spatial properties of virus spreading in 2D monolayers as well as more complex 3D environments like spheroids and organoids, potentially enabling an unprecedented look at the host-pathogen interplay through live-cell reporters of innate immunity. Conversely, these powerful imaging strategies are equally effective at much shorter length scales; for example, in measuring subcellular localization and trafficking. Thus, we anticipate that the further quantitative study of replication dynamics in the complex interplay with innate immunity and stochasticity will be broadly relevant to the study of many infectious diseases.

STAR★METHODS

Detailed methods are provided in the online version of this paper and include the following:

- KEY RESOURCES TABLE
- RESOURCE AVAILABILITY
  - Lead contact
  - Materials availability
  - Data and code availability
- METHOD DETAILS
  - Virus construction and production
  - ImmunoFISH sample preparation and staining
  - Microscopy
  - Tissue culture
  - Time-lapse image analysis
  - ImmunoFISH analysis
  - Modeling, simulations, and parameter estimates

SUPPLEMENTAL INFORMATION

Supplemental Information can be found online at https://doi.org/10.1016/j.cels.2020.12.005.

ACKNOWLEDGMENTS

Cell Systems
Article

CellPress

AUTHOR CONTRIBUTIONS

All authors conceived of and designed experiments together. Z.S.S. performed all experimental work and computational analysis. C.M.R. and T.D. supervised the research. Z.S.S. wrote the manuscript with input from all authors.

DECLARATION OF INTERESTS

REFERENCES

Adams, R.H., and Brown, D.T. (1985). BHK cells expressing Sindbis virus-induced homologous interference allow the translation of nonstructural genes of superinfecting virus. J. Virol. 54, 351–357.

Akhrymuk, I., Frolov, I., and Frolova, E.I. (2018). Sindbis virus infection causes cell death by nsP2-induced transcriptional shutoff or by nsP3-dependent translational shutoff. J. Virol. 92.

Akpinar, F., Timm, A., and Yin, J. (2016). High-throughput single-cell kinetics of virus infections in the presence of defective interfering particles. J. Virol. 90, 1599–1612.

Biryukov, J., and Meyers, C. (2018). Superinfection exclusion between two high-risk human Papillomavirus types during a Coinfection. J. Virol. 92, e01993-17.

Bratt, M.A., and Rubin, H. (1968). Specific interference among strains of Newcastle disease virus 3. Mechanisms of interference. Virology 35, 395–407.

Chalancon, G., Ravarani, C.N.J., Balaji, S., Martinez-Arias, A., Aravind, L., Jothi, R., and Babu, M.M. (2012). Interplay between gene expression noise and regulatory network architecture. Trends Genet. 28, 221–232.

Chou, Y.Y., Vafabakhsh, R., Doğanay, S., Gao, Q., Ha, T., and Palese, P. (2012). One influenza virus particle packages eight unique viral RNAs as shown by FISH analysis. Proc. Natl. Acad. Sci. USA 109, 9101–9106.

Cohen, E.M., and Kobiler, O. (2016). Gene expression correlates with the number of herpes viral genomes initiating infection in single cells. PLoS Pathog. 12, e1006082.

de Groot, R.J.d., Hardy, W.R., Shirako, Y., and Strauss, J.H. (1990). Cleavage-site preferences of Sindbis virus polyproteins containing the non-structural proteinase. Evidence for temporal regulation of polyprotein processing in vivo. EMBO J. 9, 2631–2638.

Doceul, V., Hollinshead, M., van der Linden, L., and Smith, G.L. (2010). Repulsion of superinfecting virions: a mechanism for rapid virus spread. Science 327, 873–876.

Drayman, N., Patel, P., Vistain, L., and Tay, S. (2019). HSV-1 single-cell analysis reveals the activation of anti-viral and developmental programs in distinct sub-populations. eLife 8, e46339.

Dulbecco, R. (1952a). Mutual exclusion between related phages. J. Bacteriol. 63, 209–217.

Dulbecco, R. (1952b). Production of plaques in monolayer tissue cultures by single particles of an animal virus. Proc. Natl. Acad. Sci. USA 38, 747–752.

Eaton, B.T. (1979). Heterologous interference in Aedes albopictus cells infected with alphaviruses. J. Virol. 30, 45–55.

Ellis, E.L., and Delbrück, M. (1939). The growth of bacteriophage. J. Gen. Physiol. 22, 365–384.

Fraser, D., and Kaern, M. (2009). A chance at survival: gene expression noise and phenotypic diversification strategies. Mol. Microbiol. 71, 1333–1340.

Frolova, E.I., Gorchakov, R., Pereboeva, L., Atasheva, S., and Frolov, I. (2010). Functional Sindbis virus replicative complexes are formed at the plasma membrane ▽. J. Virol. 84, 11679–11695.

Froshauer, S., Kartenbeck, J., and Helenius, A. (1988). Alphavirus RNA replicase is located on the cytoplasmic surface of endosomes and lysosomes. J. Cell Biol. 107, 2075–2086.

Garcia, J.V., and Miller, A.D. (1991). Serine phosphorylation-independent downregulation of cell-surface CD4 by nef. Nature 350, 508–511.

Grakoui, A., Levis, R., Raju, R., Huang, H.V., and Rice, C.M. (1989). A cis-acting mutation in the Sindbis virus junction region which affects subgenomic RNA synthesis. J. Virol. 63, 5216–5227.

Guo, F., Li, S., Caglar, M.U., Mao, Z., Liu, W., Woodman, A., Arnold, J.J., Wilke, C.O., Huang, T.J., and Cameron, C.E. (2017). Single-cell virology: on-chip investigation of viral infection dynamics. Cell Rep. 21, 1692–1704.

Hansen, M.M.K., Wen, W.Y., Ingerman, E., Razooky, B.S., Thompson, C.E., Dar, R.D., Chin, C.W., Simpson, M.L., and Weinberger, L.S. (2018). A post-transcriptional feedback mechanism for noise suppression and fate stabilization. Cell 173, 1609–1621.e15.

Heldt, F.S., Kupke, S.Y., Dorl, S., Reichl, U., and Frensing, T. (2015). Single-cell analysis and stochastic modelling unveil large cell-to-cell variability in influenza A virus infection. Nat. Commun. 6, 8938.

Helenius, A., Kartenbeck, J., Simons, K., and Fries, E. (1980). On the entry of Semliki Forest virus into BHK-21 cells. J. Cell Biol. 84, 404–420.

Hormoz, S., Singer, Z.S., Linton, J.M., Antebi, Y.E., Shraiman, B.I., and Elowitz, M.B. (2016). Inferring cell-state transition dynamics from lineage trees and endpoint single-cell measurements. Cell Syst. 3, 419–433.e8.

Huang, I.C., Li, W., Sui, J., Marasco, W., Choe, H., and Farzan, M. (2008). Influenza A virus neuraminidase limits viral superinfection. J. Virol. 82, 4834–4843.

Igarashi, A., Koo, R., and Stollar, V. (1977). Evolution and properties of Aedes albopictus cell cultures persistently infected with Sindbis virus. Virology 82, 69–83.

Johnson, R.M., and Spear, P.G. (1989). Herpes simplex virus glycoprotein D mediates interference with herpes simplex virus infection. J. Virol. 63, 819–827.

Johnston, R.E., Wan, K., and Bose, H.R. (1974). Homologous interference induced by Sindbis virus. J. Virol. 14, 1076–1082.

Jones, C.T., Catanese, M.T., Law, L.M.J., Khetani, S.R., Syder, A.J., Ploss, A., Oh, T.S., Schoggins, J.W., MacDonald, M.R., Bhatia, S.N., and Rice, C.M. (2010). Real-time imaging of hepatitis C virus infection using a fluorescent cell-based reporter system. Nat. Biotechnol. 28, 167–171.

Jose, J., Taylor, A.B., and Kuhn, R.J. (2017). Spatial and temporal analysis of Alphavirus replication and assembly in mammalian and mosquito cells. mBio 8, 16.

Karpf, A.R., Lenches, E., Strauss, E.G., Strauss, J.H., and Brown, D.T. (1997). Superinfection exclusion of alphaviruses in three mosquito cell lines persistently infected with Sindbis virus. J. Virol. 71, 7119–7123.

Lee, Y.-M.M., Tscherne, D.M., Yun, S.-I.I., Frolov, I., and Rice, C.M. (2005). Dual mechanisms of pestiviral superinfection exclusion at entry and RNA replication. J. Virol. 79, 3231–3242.

Lemm, J.A., and Rice, C.M. (1993a). Assembly of functional Sindbis virus RNA replication complexes: requirement for coexpression of P123 and P34. J. Virol. 67, 1905–1915.

Lemm, J.A., and Rice, C.M. (1993b). Roles of nonstructural polyproteins and cleavage products in regulating Sindbis virus RNA replication and transcription. J. Virol. 67, 1916–1926.

Lemm, J.A., Rümenapf, T., Strauss, E.G., Strauss, J.H., and Rice, C.M. (1994). Polypeptide requirements for assembly of functional Sindbis virus replication complexes: a model for the temporal regulation of minus- and plus-strand RNA synthesis. EMBO J. 13, 2925–2934.

Locke, J.C.W., and Elowitz, M.B. (2009). Using movies to analyse gene circuit dynamics in single cells. Nat. Rev. Microbiol. 7, 383–392.

Raj, A., Peskin, C.S., Tranchina, D., Vargas, D.Y., and Tyagi, S. (2006). Stochastic mRNA synthesis in mammalian cells. PLoS Biol. *4*, e309.

Raj, A., and van Oudenaarden, A. (2009). Single-molecule approaches to stochastic gene expression. Annu. Rev. Biophys. *38*, 255–270.

Ramanan, V., Trehan, K., Ong, M.-L., Luna, J.M., Hoffmann, H.-H., Espiritu, C., Sheahan, T.P., Chandrasekar, H., Schwartz, R.E., Christine, K.S., et al. (2016). Viral genome imaging of hepatitis C virus to probe heterogeneous viral infection and responses to antiviral therapies. Virology *494*, 236–247.

Razooky, B.S., Pai, A., Aull, K., Rouzine, I.M., and Weinberger, L.S. (2015). A hardwired HIV latency program. Cell *160*, 990–1001.

Rice, C.M., Levis, R., Strauss, J.H., and Huang, H.V. (1987). Production of infectious RNA transcripts from Sindbis virus cDNA clones: mapping of lethal mutations, rescue of a temperature-sensitive marker, and in vitro mutagenesis to generate defined mutants. J. Virol. *61*, 3809–3819.

Sawicki, D., Barkhimer, D.B., Sawicki, S.G., Rice, C.M., and Schlesinger, S. (1990). Temperature sensitive shut-off of Alphavirus minus strand RNA synthesis maps to a nonstructural protein, nsP4. Virology *174*, 43–52.

Sawicki, D.L., and Sawicki, S.G. (1980). Short-lived minus-strand polymerase for Semliki Forest virus. J. Virol. *34*, 108–118.

Sawicki, D.L., and Sawicki, S.G. (1993). A second nonstructural protein functions in the regulation of Alphavirus negative-strand RNA synthesis. J. Virol. *67*, 3605–3610.

Sawicki, D.L., Sawicki, S.G., Keränen, S., and Kääriäinen, L. (1981). Specific Sindbis virus-coded function for minus-strand RNA synthesis. J. Virol. *39*, 348–358.

Schönborn, J., Oberstrass, J., Breyel, E., Tittgen, J., Schumacher, J., and Lukacs, N. (1991). Monoclonal antibodies to double-stranded RNA as probes of RNA structure in crude nucleic acid extracts. Nucleic Acids Res. *19*, 2993–3000.

Schulte, M.B., and Andino, R. (2014). Single-cell analysis uncovers extensive biological noise in poliovirus replication. J. Virol. *88*, 6205–6212.

Shirako, Y., and Strauss, J.H. (1994). Regulation of Sindbis virus RNA replication: uncleaved P123 and nsP4 function in minus-strand RNA synthesis, whereas cleaved products from P123 are required for efficient plus-strand RNA synthesis. J. Virol. *68*, 1874–1885.

Shnayder, M., Nachshon, A., Rozman, B., Bernshtein, B., Lavi, M., Fein, N., Poole, E., Avdic, S., Blyth, E., Gottlieb, D., et al. (2020). Single cell analysis reveals human cytomegalovirus drives latently infected cells towards an anergic-like monocyte state. eLife *9*, e52168.

Singer, Z.S., Yong, J., Tischler, J., Hackett, J.A., Altinok, A., Surani, M.A., Cai, L., and Elowitz, M.B. (2014). Dynamic heterogeneity and DNA methylation in embryonic stem cells. Mol. Cell *55*, 319–331.

Singh, I., and Helenius, A. (1992). Role of ribosomes in Semliki Forest virus nucleocapsid uncoating. J. Virol. *66*, 7049–7058.

Singh, I.R., Suomalainen, M., Varadarajan, S., Garoff, H., and Helenius, A. (1997). Multiple mechanisms for the inhibition of entry and uncoating of super-infecting Semliki Forest virus. Virology *231*, 59–71.

Snijder, B., Sacher, R., Rämö, P., Damm, E.M., Liberali, P., and Pelkmans, L. (2009). Population context determines cell-to-cell variability in endocytosis and virus infection. Nature *461*, 520–523.

Spuul, P., Balistreri, G., Kääriäinen, L., and Ahola, T. (2010). Phosphatidylinositol 3-kinase-, actin-, and microtubule-dependent transport of Semliki Forest Virus replication complexes from the plasma membrane to modified lysosomes. J. Virol. *84*, 7543–7557.

Steck, F.T., and Rubin, H. (1966). The mechanism of interference between an avian leukosis virus and Rous sarcoma virus. II. Early steps of infection by RSV of cells under conditions of interference. Virology *29*, 642–653.

Stiles, K.M., Milne, R.S.B., Cohen, G.H., Eisenberg, R.J., and Krummenacher, C. (2008). The herpes simplex virus receptor nectin-1 is down-regulated after trans-interaction with glycoprotein D. Virology *373*, 98–111.

Stollar, V., and Shenk, T.E. (1973). Homologous viral interference in Aedes albopictus cultures chronically infected with Sindbis virus. J. Virol. *11*, 592–595.

Strauss, J.H., and Strauss, E.G. (1994). The alphaviruses: gene expression, replication, and evolution. Microbiol. Rev. *58*, 491–562.

Taylor, R.M., and Hurlbut, H.S. (1953). The isolation of Coxsackie-like viruses from mosquitoes. J. Egypt. Med. Assoc. *36*, 489–494.

Taylor, R.M., Hurlbut, H.S., Work, T.H., Kingston, J.R., and Frothingham, T.E. (1955). Sindbis virus: a newly recognized arthropodtransmitted virus. Am. J. Trop. Med. Hyg. *4*, 844–862.

Wang, Y.F., Sawicki, S.G., and Sawicki, D.L. (1991). Sindbis virus nsP1 functions in negative-strand RNA synthesis. J. Virol. *65*, 985–988.

Whitaker-Dowling, P., Youngner, J.S., Widnell, C.C., and Wilcox, D.K. (1983). Superinfection on exclusion by vesicular stomatitis virus. Virology *131*, 137–143.

Zebovitz, E., and Brown, A. (1968). Interference AMONG group A arboviruses. J. Virol. *2*, 1283–1289.

Zeng, L., Skinner, S.O., Zong, C., Sippy, J., Feiss, M., and Golding, I. (2010). Decision making at a subcellular level determines the outcome of bacteriophage infection. Cell *141*, 682–691.

Zou, G., Zhang, B., Lim, P.Y., Yuan, Z., Bernard, K.A., and Shi, P.Y. (2009). Exclusion of West Nile virus superinfection through RNA replication. J. Virol. *83*, 11765–11776.

Cell Systems
Article

          CellPress

STAR★METHODS

KEY RESOURCES TABLE

REAGENT or RESOURCE	SOURCE	IDENTIFIER
Antibodies		
J2	Scicons	Cat# 10010200; RRID:AB_2651015
Goat anti-Mouse Alexa Fluor 647 Secondary Antibody	Molecular Probes	Cat# A-21235; RRID:AB_2535804
Bacterial and virus strains		
Toto1101	This lab	N/A
Toto1101/nsP3-mCitrine	This paper	N/A
Toto1101/nsP3-mTurquoise2	This paper	N/A
Chemicals, peptides, or recombinant proteins		
Dextran Sulfate	Fisher Scientific	Cat# BP1585-100
E.coli tRNA	Roche	Cat# 10109541001
Formamide	ThermoFisher	Cat# AM9342
Ribonucleoside Vanadyl complex	NEB	Cat# S1402S
20X SSC	Invitrogen	Cat# 15557044
10% Normal Goat Serum	Thermo	50062z
CellMask Red CMTPX	Invitrogen	C34552
NucRed	Invitrogen	R37106
NucBlue	Invitrogen	R37605
Experimental models: cell lines		
BHK-21	ATCC	Cat# CCL-10
Oligonucleotides		
Plus-strand smFISH Probes	This paper	Table S1
Minus-strand smFISH Probes	This Paper	Table S1
Primers for cloning virus reporters and mutants	This Paper	Table S2
Software and algorithms		
Live-cell tracking software	Hormoz et al., 2016	N/A
Dot-detection software	Hormoz et al., 2016	N/A
Scripts and accompanying data for figures reported here	This Paper	https://github.com/zsinger/Singer_CellSystems_2020
Matlab 2019b	MathWorks	https://www.mathworks.com

RESOURCE AVAILABILITY

Lead contact
Further information and requests for resources and reagents should be directed to and will be fulfilled by the Lead Contact, Charles M. Rice ricec@rockefeller.edu

Materials availability
Viruses generated in this paper can be requested from the lead author.

Data and code availability
- Raw movies and smFISH snapshots can be requested from the lead contact. Quantification of fluorescence measurements is available at https://github.com/zsinger/Singer_CellSystems_2020.
- This paper does not report original code.
- The scripts used to generate figures (and accompanying data files) are available at https://github.com/zsinger/Singer_CellSystems_2020
- Any additional information required to reproduce this work is available from the Lead Contact.

METHOD DETAILS

Virus construction and production

Sindbis virus from Toto1101 (Rice et al., 1987; Grakoui et al., 1989) was transcribed *in vitro* using mMessage mMachine SP6 Transcription Kit (Ambion AM1340) for 2hrs, followed by DNAse Digestion for 20 min, and subsequently purified using RNEasy Mini Kit (Qiagen 74104). 500ng RNA was transfected into BHK-21s using Lipofectamine MessengerMax (Lifetech LMRNA001) in wells of a 24 well plate and passaged twice for expansion. Inoculations were performed for 20–30 min in 1%FBS in PBS with Calcium and Magnesium. Virus was concentrated using Amicon Ultra-15 Centrifugal Filter Concentrators (Millipore UFC910008). Virus was titered by plaque assay, and by fluorescence imaging to identify where ~50% of cells were infected for determination of MOI 1, 5hpi.

To construct reporter viruses, Toto1101 was digested with SpeI, and Gibson assembled with fluorescent proteins mCitrine and mTurquoise2 PCR'd with homology to surrounding the SpeI cut sites. Mutants of nsP2 and nsP3 were constructed through digestion of Toto1101 by ClaI and AvrII, and each re-assembled by Gibson with a pair of amplicons off Toto1101 using mutagenic primers introducing the required changes. These primers are listed in Table S2.

ImmunoFISH sample preparation and staining

Plus strand FISH probes were designed to bind over nsP1 and nsP2 sequences, which therefore exclude subgenomic RNA. Minus strand probes were targeted against the complement of nsP3 and nsP4 (Table S1). Cells were fixed in 4% formaldehyde for 5 min at room temperature, washed twice in PBS, and placed in 70% ethanol overnight at -20°C. The next morning, cells were washed twice with PBS; permeabilized in 0.1% TritonX for 5 min; washed twice in PBS; blocked in 10% Normal Goat Serum (Thermo 50062Z) treated with RNASecure (Invitrogen AM7005) for 30 min; washed twice with PBS; incubated with J2 primary-antibody (Scicons 10010200) at 0.5ug/ml in 10% Normal Goat Serum (treated with RNASecure) for 2 h; washed twice with PBS; incubated with goat anti-Mouse Alexa Fluor 647 secondary antibody (Invitrogen A-21235) at RT for 30 min; washed twice in PBS and incubated with 10% Normal Goat Serum treated with RNASecure for an additional 10 min at RT; washed twice in PBS; postfixed in 4% formaldehyde for 5 min at RT; washed twice with PBS; equilibrated in FISH Wash Buffer containing 2X SSC (Invitrogen 15557044) and 20% Formamide (Ambion AM9342) for 5min at RT; and hybridized with Stellaris FISH probes labeled with Quasar 570 or Quasar 670 at 125nM (Biosearch Technologies, Table S1) overnight at 30°C in Hybridization Buffer (containing 20% Formamide (Ambion AM9342), 2X SSC, 0.1g/ml Dextran Sulfate (Fisher Sci BP1585-100), 1mg/ml E.coli tRNA (Roche 10109541001), 2mM Vanadyl ribonucleoside complex (NEB S1402S), and 0.1% Tween 20 (VWR 97062-332) in nuclease free water). The next morning, the hybridization buffer was removed and cells were washed twice in FISH Wash Buffer; incubated in FISH Wash Buffer without probe for 30min at 30°C; washed three times with 2X SSC; counterstained with DAPI; and finally imaged in 2X SSC.

In the experiment to determine whether minus-strand probes could bind to dsRNA disrupted by sodium hydroxide, samples were washed twice in ddH$_2$O, after fixing and PBS washing, then treated for 30s with 50mM NaOH and then washed three times in PBS. After this, the standard smFISH protocol was followed.

Microscopy

Cells were imaged on a Nikon Ti2 with PFS4, a Nikon Motorized Encoded Stage, Lumencor SpectraX Light Engine, custom Semrock filters, and a Prime 95B sCMOS camera. Automated acquisition for snapshots and time-lapse was programmed in NIS Elements. The scope was equipped with an OKO stagetop incubator with temperature-, humidity-, and CO$_2$-control, enabling long-term imaging. ImmunoFISH utilized a 60x objective, and time-lapse a 20X ELWD objective.

Tissue culture

BHK-21s (ATCC CCL-10) were grown at 37°C and 5% CO$_2$ in DMEM/F12 with GlutaMax and Sodium Pyruvate (Gibco 10565018), supplemented with 10% FBS (Gibco 10437028, Lot 1780025), and NEAA (Gibco 11140050). For live-cell imaging of BHKs, DMEM/F12 was replaced with FluoroBrite DMEM (Gibco A1896701). For segmentation purposes for live cell imaging, BHKs were additionally stained with 1uM CellMask Red CMTPX cytoplasmic dye (Invitrogen C34552) for 10min at room temperature followed by three washes with PBS prior to imaging, and with 3ul/ml NucRed nuclear dye (Invitrogen R37106) or 5ul/ml NucBlue (Invitrogen R37605).

Time-lapse image analysis

All image- and data-analysis was performed in MATLAB 2019b using custom-built scripts. Single-cell tracking code was developed in the Elowitz Lab (Hormoz et al., 2016), and modified for use with cytoplasmic cell segmentation. BHK's which maintain large and irregular cytoplasmic boundaries require two markers, one nuclear and one cytoplasmic, for use in a seeded watershed segmentation algorithm. A movie of one well with no cells but all media and staining components is used to background correct sample wells at each corresponding time-point. Total fluorescence over the segmented area is summed to yield total fluorescence.

Cell Systems
Article

CellPress

ImmunoFISH analysis

Two-channel segmentation is performed for immunoFISH using the same algorithm as in time-lapse imaging, but where autofluorescence on the 594 channel replaces the CellMask Red CMTPX dye as a cytoplasmic marker. Cells were imaged over a 6um z-stack every 2um; then a maximum-intensity projection was used for analysis. Puncta are identified using a Laplacian-of-Gaussian convolution as previously described (Raj et al., 2006; Singer et al., 2014) on which a threshold is defined by an uninfected sample. Total fluorescence is analogously summed over the cell area.

Modeling, simulations, and parameter estimates

Logistic growth of the virus is modeled as

$$\frac{dV}{dt} = rV\left(1 - \frac{V}{K}\right)$$

(Equation 1)

where parameters r and K are the replication rate and carrying capacity, respectively.

To estimate parameters from single infection experiments, we first subtract the initial fluorescence values and set the starting value equal to the MOI of the experiment. Then we rescale the median of the endpoints to be 200,000, or the number of copies of full-length plus-strand previously estimated in the literature (Wang et al., 1991). Finally, each trace is aligned so that its maximum slope occurs at the mean τ for the sample. These individual traces are then used in least squares curve fitting on the solution to Equation 1, where K and r were allowed to vary, and the initial condition was fixed at the empirically determined MOI. On average, the slope over the last 3 h was $\sim$95% reduced from their maximum production rates (Figure 3H). In fitting these traces to logistic growth, we selected only those whose final slope changed $\leq$ 15% over the last three hours of the experiment (black lines in Figure S3D; excluded traces are shown in gray). The estimated growth trace is shown as the heavy dashed line in Figure S3D.

Competitive Lotka-Volterra growth is modeled for virus 1 and 2 (V_1 and V_2, respectively) as:

$$\frac{dV_1}{dt} = rV_1\left(1 - \frac{V_1 + \alpha_{12}V_2}{K}\right)$$

(Equation 2)

$$\frac{dV_2}{dt} = rV_2\left(1 - \frac{\alpha_{21}V_1 + V_2}{K}\right)$$

(Equation 3)

where the replication rate r is assumed to be the same for both viruses, and have a shared carrying capacity, K. Note that the coefficients $\alpha_{12} = \alpha_{21} = 1$, a regime where there is no additional inhibitory effect of one virus on the other beyond their equal contribution towards their shared carrying capacity.

In all Figures, the data presented are representative of at least two independent experiments.